

Pair production tomography imaging

Qihui Lyu

University of California, Los Angeles

Ryan Neph

University of California, Los Angeles

Ke Sheng (✉ ksheng@mednet.ucla.edu)

University of California, Los Angeles

Article

Keywords: X-ray Computed Tomography (CT), filtered back projection (FBP), time-of-flight (TOF), canning pencil beam (SPB)

Posted Date: March 8th, 2021

DOI: <https://doi.org/10.21203/rs.3.rs-151960/v1>

License:   This work is licensed under a Creative Commons Attribution 4.0 International License.

[Read Full License](#)

Version of Record: A version of this preprint was published at Nature Biomedical Engineering on October 24th, 2022. See the published version at <https://doi.org/10.1038/s41551-022-00953-8>.

Pair production tomography imaging

Qihui Lyu, Ryan Neph, Ke Sheng

Department of Radiation Oncology, University of California Los Angeles, Los Angeles, CA,
90095, USA

X-ray Computed Tomography (CT) is an exceptionally versatile tool for diagnosis and detection. Despite numerous technological evolutions, the underlying mechanism for CT image formation has not changed. To markedly expand beyond the current capacity of X-ray CT based on a new image formation mechanism, we introduce pair production tomography (P²T) imaging. Unlike CT, whose signals arise from attenuation of the incident photons, P²T collects coincident annihilation photons originated from the pair production interaction with high energy X-rays for tomographic reconstruction. We studied three P²T acquisition methods, including filtered back projection (FBP), time-of-flight (TOF), and scanning pencil beam (SBP). Using Monte Carlo simulation on phantom and patient data, we demonstrate three distinctly new and desirable capabilities for P²T: high linearity with the material atomic number for element mapping and soft tissue differentiation, the ability to form tomography with as few as a single heavily truncated X-ray beam, and in vivo radiotherapy treatment dose verification and monitoring. Among the three P²T acquisition methods, FBP is the least technically demanding, but its utility is limited to high radiation dose procedures such as radiotherapy treatment monitoring. Both TOF and SBP result in high signal-to-noise ratio (SNR) P²T images with a typical imaging dose. The quality of TOF relies on the time resolution of detectors. In comparison, SBP suppresses localization errors based on the known excitation path, which significantly mitigates the detector time resolution requirement.

There is a long history of using X-rays for detection. Besides industrial inspection, X-rays hold a uniquely important position in medicine. Compared with other medical imaging techniques such as magnetic resonance imaging (MRI)¹⁻³ and Positron emission tomography (PET)⁴, X-ray imaging systems are advantageous in their low cost, high speed, high resolution, and high sensitivity to dense or high-atomic number materials. A major breakthrough in X-ray imaging is the invention of tomographic images. By acquiring the 1D linear or 2D planar projection images from many different angles around the patient, a 3D Computed Tomography (CT)^{5,6} image can be reconstructed^{7,8}. CT revolutionized modern medicine by enabling diagnoses that were simply impossible before, such as early-stage lung cancer screening⁹.

Since CT's invention, many technological developments in the hardware and reconstruction methods have significantly improved its speed, image quality, and versatility. Nonetheless, the underlying mechanism for image formation remains the same. X-ray imaging signals are produced by a mixture of physical interactions, including Rayleigh scatter, photoelectric effect, and Compton scatter. These fundamentally different interactions result in different attenuation patterns with regard to the material properties. The problem is further complicated by the bremsstrahlung poly-energetic X-rays commonly available for diagnosis and therapy. As a result, it is difficult to obtain clean material information from the X-ray CT images. Another weakness of CT is poor soft-tissue contrast due to the similarity in densities and the diminishing photoelectric effect with low atomic number materials. For tomographic reconstruction, attenuation signals from sufficient X-ray beam angles are required. In specific cases, with machine learning¹⁰ and sparse regularization¹¹ methods, the requirement can be relaxed to predict useable images, but a general solution for sparse-view tomographic image reconstruction does not exist¹². Furthermore, CT reconstruction based on the Radon transform has global support, meaning that truncated projections with a partial view of the patient would inevitably introduce inaccuracies, whose magnitude depends on the degree of truncation and reconstruction method. One undesired consequence of the data sufficiency requirement is the exposure of a large patient volume to the imaging dose regardless of the region-of-interest size.

Another major application of X-rays in modern medicine is radiotherapy of cancer. The ionizing radiation from high-energy X-rays can break DNA strands, which, if not repaired, leads to cell death. By exploiting the differential repair mechanisms of cancer and normal cells, and the additional therapeutic contrast due to conformal dose distribution, radiotherapy has been a mainstay modality in cancer treatment. It is estimated that 60% of cancer patients and 40% of the curative cases in the US use radiotherapy as either one of or the only treatment method¹³.

X-ray based radiotherapy is an open-loop treatment, meaning that the delivered 3D dose in the patient is not directly verified. Compared with a closed-loop system, an open-loop system is intrinsically less safe and less accurate due to the lack of direct feedback. In-vivo radiation dose deep inside the patient's body is difficult to measure. Implanted dosimeters require an undesirable interventional procedure and still only measure point doses¹⁴. Cerenkov imaging is limited to superficial locations¹⁵. X-ray induced acoustic CT (XACT) has shown the promise to

measure 3D in-vivo dosimetry. However, XACT applications are hampered by the acoustic boundaries, low resolution and signal-to-noise ratio (SNR), and mandatory ultrasound receiver arrays that interfere with X-ray beam path¹⁶. Because of the fundamental impediments, these in-vivo dosimetry methods are unlikely to meet 3D in-vivo dosimetry's general needs to close the radiotherapy open-loop.

To meet the challenges and expand X-ray tomography's applicability, we introduce a distinctly new X-ray image formation method, namely pair production tomography (P²T) imaging. Instead of using the transmission data of X-ray beams in CT, P²T collects the coincident annihilation photons originated from mega-voltage X-rays induced pair productions. P²T provides a different contrast than CT, a clean linear relationship to the material atomic number, and direct verification of radiotherapy dose, even with partial-view and sparse-view projections.

Principles of pair production tomography imaging

Figure 1a illustrates the major X-ray interactions in the P²T energy range (e.g., 10 MV bremsstrahlung source, which is commonly used in radiotherapy). In the photoelectric effect, an incident photon vanishes after striking a bound electron, resulting in the ejection of the electron and a vacancy in the inner shell. To stabilize the atom, an outer shell electron fills the vacancy and converts the energy lost to characteristic radiation X-ray or as an Auger electron. In Compton scattering, an incident photon is scattered by a charged particle, typically an electron, and transfers part of the photon energy to the recoiling electron. The pair production occurs in a Coulomb force field, typically near a nucleus, where an incident X-ray of sufficiently high energy (at least 1.022 MeV) is annihilated and produces a positron and an electron. Subsequently, the electron dissipates energy through successive interactions with the medium before being absorbed by the medium. However, as the positron loses its kinetic energy and comes to a near stop, it comes into contact with an electron with nearly simultaneous annihilation of the positron and the electron and their conversion into two annihilation photons moving in opposite directions with an energy of around 511 keV. The pair production cross-section is linear to the material atomic number¹⁷.

The P²T formation process is illustrated in Figure 1b. An X-ray beam typically used for radiotherapy introduces the pair production photons in a subject placed at the center of a ring-detector array. Two time-coincident 511 keV photons traveling in opposite directions are captured by two detectors in the ring. A 3D map of the event locations can then be reconstructed based on a collection of the signals.

The photon contamination from photoelectric and Compton interactions are effectively reduced via a coincidence time window and an energy window. Figure 1c shows the energy distribution of detected photons ranging from 0 to 1 MeV, with a zoom-in view of 0.511 MeV \pm 10% energy range (Figure 1d,e). The 511 keV photons consist 0.91%, 15.4%, and 77.6% of the total photons, before applying filters (Figure 1c), after applying an \pm 10% energy window filter (Figure 1d), and

after applying the $\pm 10\%$ energy and 1 ns coincidence time filters (Figure 1e), respectively.

Two P²T approaches are investigated in this study (Figure 1f). The volume imaging approach is similar to CT imaging, where the entire imaging Field-of-View (FOV) is imaged simultaneously for each view angle. In scanning pencil beam (SPB) imaging, the imaging FOV is excited sequentially. SPB affords additional geometrical information for tomographic reconstruction by pinpointing the pair production location at the intersection of the pencil beam and the detector coincidence line.

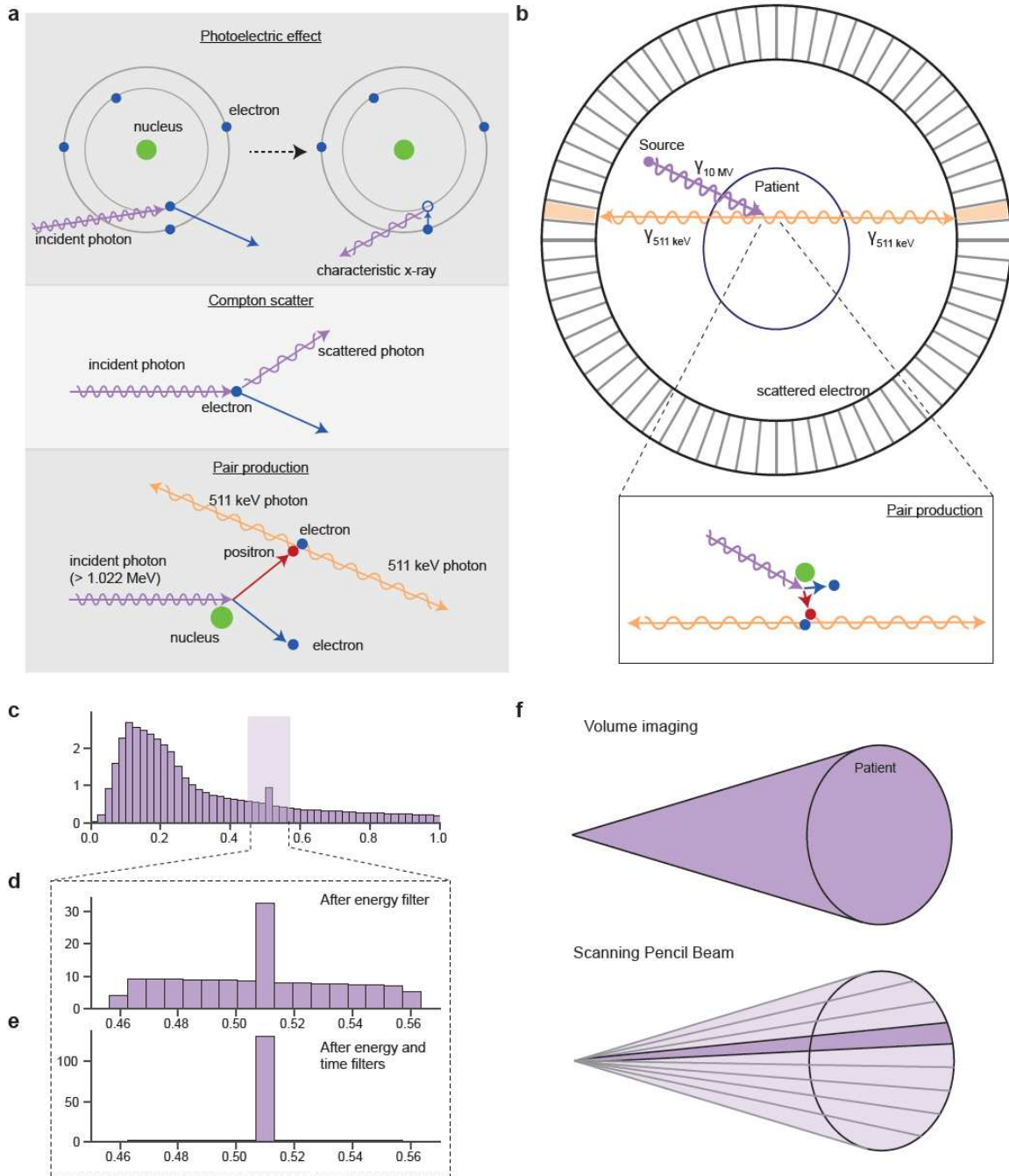


Figure 1 (a) Illustration of the photoelectric effect, Compton scatter, and pair production interaction. (b) Illustration of pair production tomography imaging (P²T) formation process. (c) The energy distribution of detected photons ranging from 0 to 1 MeV, (d) The energy distribution of detected photons after applying an $\pm 10\%$ energy window filter, (e) The energy distribution of detected photons and after applying the $\pm 10\%$ energy and 1 ns coincidence time filters. (f) Comparison of volume imaging and scanning pencil beam (SPB) imaging.

Simulation, reconstruction, and post-processing

A general-purpose Monte Carlo (MC) package, Geant4¹⁸, was used to characterize P²T. A ring-detector array with a total of 1440 detector elements and a diameter of 240 cm were assumed.

For simplicity, we set the ring-detector to have only a single row with 10 cm width in the z-direction (e.g., patient superior-inferior direction), which covers 4.17% of the 4π solid angles. We assumed a $\pm 10\%$ energy window. The photon detection time can be computed as the sum of the photon releasing time, the photon traveling time, and the detector response time. The primary photons within each pencil beam are released in sequence with time intervals following a uniform distribution. The detector response time is simulated as a Gaussian distribution with a standard deviation equal to the time resolution of the detector. We considered two cases: time resolution of 20 ps or 300 ps, representing the upper limits of experimental Cerenkov^{19,20} and state of the art commercial scintillator detectors²¹, respectively.

Coincident events were identified as two energy-eligible photons (within the energy window) arriving at two detector-elements within the coincidence time 1 ns. Two coincident events define a Line-Of-Response (LOR): the line connecting the two detector-elements, indicating that the annihilation event happened on the LOR. Once LORs are identified, they are rebinned to sinogram and then reconstructed using Filtered Back Projection (FBP) with the Michigan Image Reconstruction Toolbox (MIRT)²². With the known excitation path, the SPB based reconstruction locates each annihilation event as the intersection of the corresponding LOR and the SPB. For detectors with a high time resolution (e.g., 20 ps), the range of the annihilation event along the LOR can be narrowed down according to the time-of-flight (TOF) of the two photons. In addition to the reconstructed images, the ground-truth image was created as the voxel-wise tally of positron annihilation events.

Similar to PET, the attenuation to annihilation photons is compensated by weighting the coincident photon pair counting based on their respective radiological pathlengths. Besides attenuation, the signal intensity of P²T also depends on the fluence intensity of the imaging beams. For quantitative imaging, the P²T images are normalized by the fluence to correct the bias due to variation in the excitation X-ray beam fluence.

A summary of the correction methods, imaging approaches, and the assumed detector time resolution used for all P²T images can be found in Table 1.

Applications	Correction methods	Reconstruction			
		GT	FBP	SPB	TOF
Quantitative Imaging	Attenuation correction	No	Yes	Yes	Yes
	Fluence correction	Yes	Yes	Yes	Yes
Radiotherapy	Attenuation correction	No	Yes	NA	Yes
	Fluence correction	No	No	NA	No
Imaging approaches		Both	VI	SPB	VI
Detector time resolution		NA	300 ps	300 ps	20 ps

Table 1 A summary of the correction methods, imaging approaches, and the assumed detector time resolution. The imaging approaches include scanning pencil beam (SPB) imaging, volume imaging (VI), or both. NA means Not Applicable.

P²T linearity with high Z elements

Both the CT and P²T image intensities are determined by the cross-section of physical interactions, or the attenuation coefficient, which is a function of the atomic number Z , the density ρ , and the photon energy $h\nu$.

In P²T with MV X-ray as the source, both Compton scatter and pair production contribute to the interaction. However, since the P²T detectors remove the majority of Compton scatter photons, the P²T image intensity overwhelmingly depends on the probability of pair production interaction, which is linearly proportional to ρZ . Therefore, in theory, P²T image contrast also follows a simple linear relationship with ρZ .

In comparison, the CT image signals using a kV source are produced by a mixture of Rayleigh scatter, photoelectric effect, and Compton scatter that is both material and energy-dependent. The Compton attenuation coefficient is approximately Z independent, and the photoelectric effect is approximately proportional to Z^3 with sharp discontinuities at the K-edges. The convolution of poly-energetic X-rays with non-linear cross-intersections inevitably renders multiple material differentiation tasks an underdetermined problem.

The linearity of P²T contrast to Z is evaluated on an elliptical water-equivalent phantom 10 inserts, among which 7 inserts are made of water and 5% of high- Z elements (ranging from 53 to 83), including Iodine, Barium, Gadolinium, Ytterbium, Tantalum, Gold, and Bismuth. The minor and major axes of the phantom are 20 cm and 24 cm, respectively. P²T MC simulation utilized a total of 56.6 billion primary particles in 20 equally distributed coplanar fan beams. The pencil beam size for SPB delivery is $0.2 \times 0.2 \text{ cm}^2$. MC CT simulation utilized a total of 72 billion primary particles in 360 equally distributed coplanar fan beams. The CT detector pixel size is 0.2 cm by 0.2 cm, the source to detector distance is 100 cm, and the source to isocenter distance is 66.7 cm. The beam energies of P²T and CT are 10 MV and 120 kVp, respectively. 10 MV X-rays have a typical poly-energetic bremsstrahlung X-rays spectrum for radiotherapy. 120 kVp X-ray

spectrum is typical from a diagnostic hot cathode system. The reconstructed image resolution is 0.2 cm.

The CT image and the P²T images are presented in Figure 2a and Figure 2c, respectively. Linear regression of the increased contrast to water on the atomic number Z is presented in Figure 2b. The CT has a higher contrast for the high Z materials due to the Z³ photoelectric cross-section, but the relationship between CT image intensity and the atomic number is non-linear. For example, although the Gadolinium has a lower atomic number than Ytterbium, Tantalum, Gold, and Bismuth, its K-edge energy at 50 keV is closer to the peak of the 120 kVp CT spectrum. Consequently, the CT contrast of Gadolinium is substantially higher than other materials. In comparison, the P²T image intensities show the expected linear relationship with the atomic number. The r² values of CT, P²T ground truth image, P²T FBP, P²T SPB, and P²T TOF are 0.23, 0.99, 0.48, 0.93, 0.84, respectively. Apart from P²T FBP, where the image contrast is obscured by excessive noise, all other P²T images show a strong linear relationship with Z.

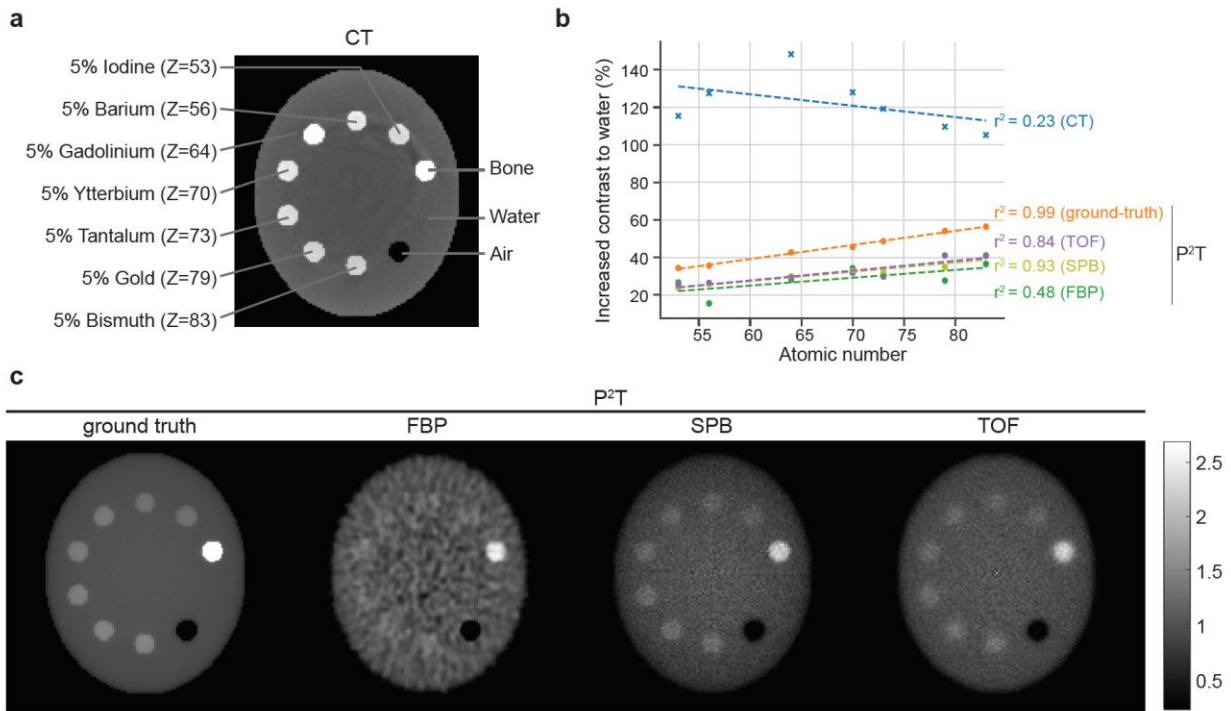


Figure 2 (a) The CT image of a nanoparticle phantom with 10 inserts, among which 7 inserts are made of water and 5% of high-Z elements, including Iodine, Barium, Gadolinium, Ytterbium, Tantalum, Gold, and Bismuth. (b) The relative increase in contrast to water is evaluated for the 7 inserts for the CT image and all P²T images. Linear regression of the increased contrast on the atomic number Z was performed for all images. (c) Comparison of P²T ground truth image, P²T image from FBP reconstruction, P²T image from SPB based reconstruction, and P²T image from TOF reconstruction. All images were normalized such that the intensity of the water insert is 1.

P²T linearity with tissue equivalent materials

Besides high Z nanoparticle imaging, P²T for human tissue imaging is evaluated on the same elliptical phantom containing 10 different tissue-mimicking inserts, including air, lung inhale,

lung exhale, adipose, breast, water, muscle, liver, trabecular bone, and dense bone (Figure 3a), under the same geometry and energy setup. Figure 3b shows the image contrast of the P²T from different reconstruction methods compared with CT on the standard phantom, with error bars showing the standard deviations. The dashed lines show the theoretical values of P²T contrast, defined as the increments in ρZ_{eff} of each material in relative to water, where ρ is the material density and Z_{eff} is the effective atomic number of a composite material²³ (Table 2 in the supplementary materials). The ground-truth and reconstructed P²T images and the CT image are shown in Figure 3c.

Among the three P²T reconstruction methods, FBP provides the lowest SNR, making it more difficult to discern materials with similar ρZ_{eff} to water. The SPB image is comparable to the TOF image without requiring a high detector time resolution. The SPB and TOF images are noisier than the ground-truth image due to the low detector coverage of the solid angles.

For low Z materials, the photoelectric component in CT is negligible, and the contrast is approximately linear to ρ , while P²T contrast is linear to ρZ_{eff} . The Z_{eff} factor offers greater contrast for materials including the lung inhale, lung exhale, adipose, and breast tissue. As an example, the breast tissue has a 1% difference in density to water but a 13.6% difference in Z_{eff} , which translates to a 13.6 \times increase in the contrast using P²T.

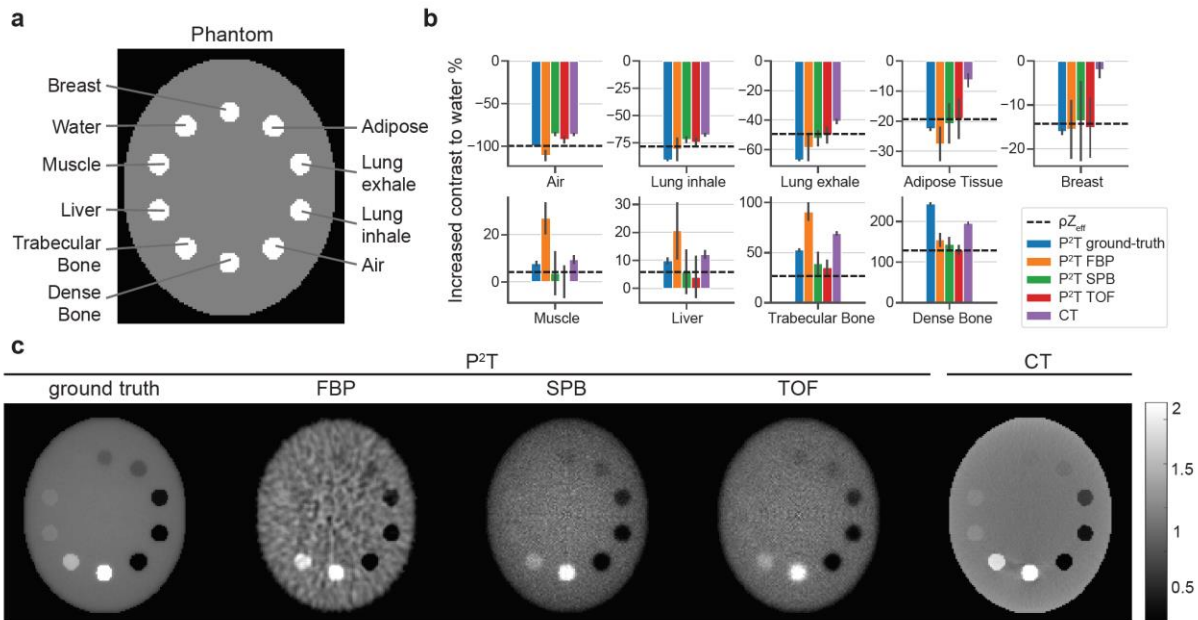


Figure 3 (a) The standard phantom with 10 inserts, including air, lung inhale, lung exhale, adipose, breast, water, muscle, liver, trabecular bone, and dense bone. (b) The relative increase in contrast to water is evaluated for all materials but water, with error bar showing standard deviations. The dashed lines show the increments in ρZ_{eff} of each material in relative to water. (c) Comparison of P²T ground truth image, P²T image from FBP reconstruction, P²T image from SPB based reconstruction, P²T image from TOF reconstruction, and CT image. All images were normalized such that the intensity of the water insert is 1.

P²T allows partial-view and sparse-view imaging

The data sufficiency condition of P²T is distinctly different from CT, which requires the voxel to be reconstructed on the line connecting two points on the source trajectory²⁴. The requirement is translated into densely sampled full view projections around the image subject. P²T is intrinsically compatible with partial-view, and sparse-view imaging as the pair production event detections are separable from each other. Even with locally irradiating a Region-of-Interest (ROI), P²T can extract information from an interior patient sub-volume.

Figure 4a shows a comparison of 20-beam full-view P²T images (top) and 2-beam partial-view P²T images (bottom). The ROI, in this case, are the three inserts (5% Iodine, Ytterbium, and Bismuth from left to right) at the bottom of the phantom. The full-view P²T simulation utilized a total of 56.6 billion primary particles in 20 equally distributed coplanar beams with full coverage of the phantom in each beam. The partial-view P²T utilized a total of 10.6 billion primary particles in 2 opposing beams with partial beam coverage as indicated by the yellow lines. Despite irradiating only 20% of the whole volume and using only two beams, the 2-beam partial-view images are comparable to the 20-beam full-view P²T images within the ROI. More importantly, the imaging dose is limited to the irradiated volume. In the specific case, the maximal imaging dose is around 3.3 cGy, assuming 100% detector efficiency.

Figure 4b shows the image intensity of the 3 inserts normalized by their average values. The ground truth, SPB, and TOF images show similar image intensity values between the 2-beam partial-view images and the 20-beam full-view images. The variations in the FBP images is due to statistical imaging noise.

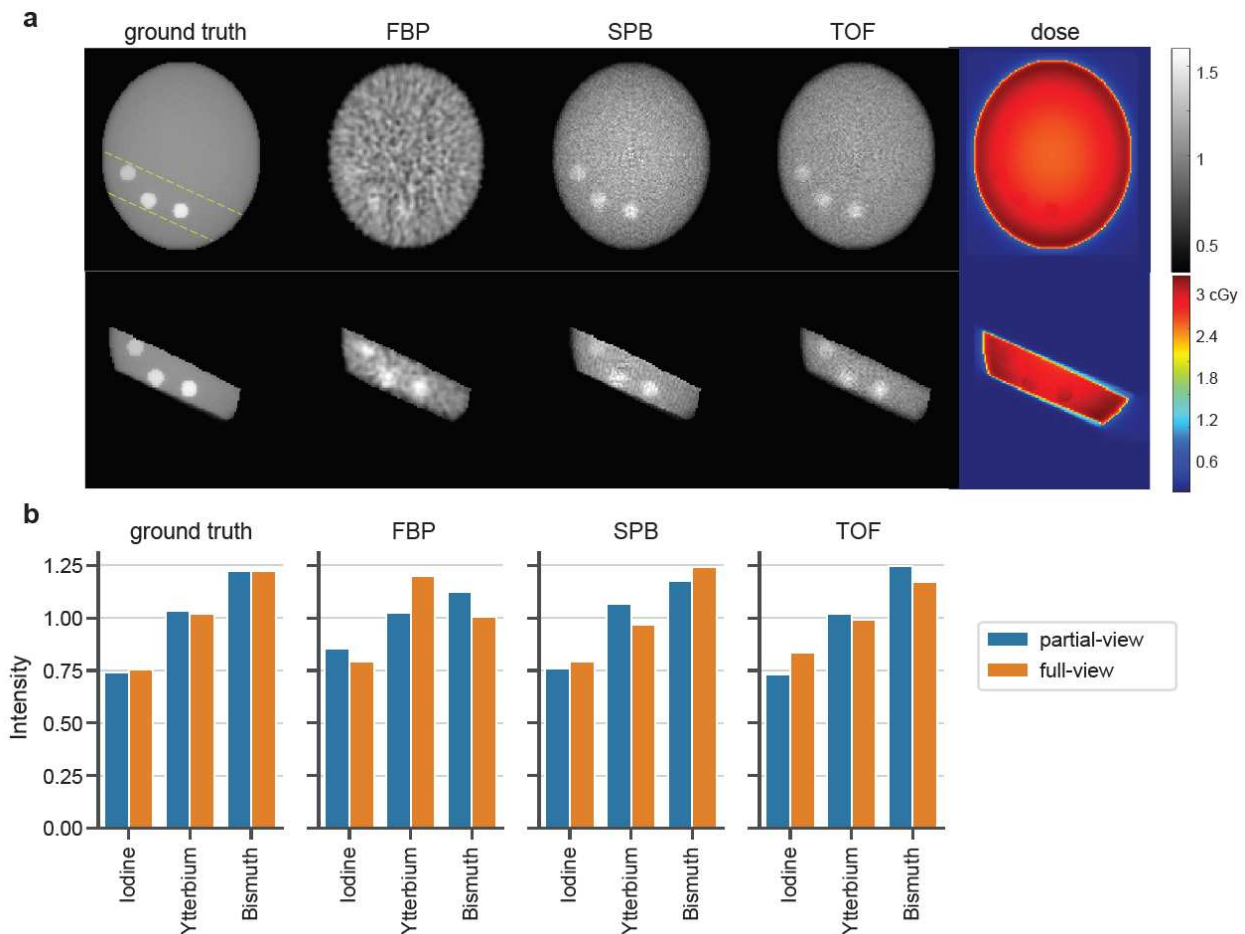


Figure 4 (a) Comparison of 20-beam full-view P^2T images (top) and 2-beam partial-view P^2T images (bottom), including ground truth image, P^2T image from FBP reconstruction, P^2T image from SPB based reconstruction, and P^2T image from TOF reconstruction. All images were normalized such that the intensity of the water insert is 1. The three inserts in the partial-view are Iodine, Ytterbium, and Bismuth from left to right. (b) The image intensity of the 3 inserts normalized by their average values for both full-FOV P^2T images and partial-view P^2T images.

Real-time patient radiation dose monitoring

Radiotherapy treatment uses high-energy X-rays (e.g., 10MV X-rays) to kill cancer cells. The same energy beams are conducive for P^2T . The radiotherapy dose is closely related to a quantity termed TERMA, the Total Energy Released per unit Mass. TERMA is the energy loss of primary photons as they interact in the medium. TERMA is proportional to the fluence intensity, the energy of the primary photon, and the total attenuation coefficient. The radiation dose is the local energy deposition from ionizing radiation, which can be computed as a local convolution of TERMA with energy deposition kernels²⁹ to account for the dose spread under different materials and photon energies. The number of pair production interactions is proportional to the fluence intensity and the pair production attenuation coefficient. The P^2T images, defined as the

number of annihilation events, show the number of pair production interactions convoluted with the positron traveling.

We tested the feasibility of obtaining P²T images using pair production signals produced by radiotherapy beams on a glioblastoma multiforme (GBM) cancer case. The dose calculation was performed using Geant4 for an intensity-modulated radiotherapy plan with 7-equal-spacing coplanar beams. The pencil beam size for dose calculation was 0.5×0.5 cm². The dose voxel size was 0.25×0.25×0.25 cm³. The dose calculation simulated 10⁸ particles within each pencil beam. A dose matrix was constructed based on the dose calculation result, which converts the x-ray fluence intensity to dose distribution within the patient body. The dose matrix was used to create a treatment plan for the Intensity-Modulated Radiotherapy (IMRT) delivery technique^{25,26}, where the radiation dose distribution was optimized to achieve conformal dose within the target volume and minimize dose to the surrounding normal tissues, using convex optimization algorithms^{27,28}.

The treatment plan optimization produces an optimized fluence map, dictating the number of particles in each pencil beam to achieve the optimized treatment plan. Assuming the detector efficiency is 10% to collect a coincident photon pair, we simulated 10% of the particles needed to deliver a 2Gy fraction treatment, which amounts to a total of 221.2 billion primary particles.

The radiotherapy treatment dose (Figure 5a) and the TERMA (Figure 5b) are compared with P²T images (Figure 5c). The image resolution is 0.25×0.25 cm². All images were normalized by the mean intensity value within the target and were displayed as iso-intensity color-wash images superimposed on the CT image. The target and normal tissues are contoured with different colors. Through optimization, the radiation dose was pushed towards the prescription dose 2Gy within the target and was tailored to avoid important normal tissues, including the brainstem, chiasm, eyes, and etc. Figure 5d shows the cumulative Intensity Volume Histograms (cIVHs) of dose, TERMA, and P²T ground truth. The cIVH lines indicate the volume percentage of a structure receiving intensity values greater than a threshold.

As closely linked physical quantities, the dose, TERMA, and P²T are also correlated, as shown in the intensity maps and the cIVH lines. The highest intensity values are achieved within the target and the ring structure (a 1.5 cm shell surrounding the target). Sparing of normal tissues, including the brainstem, eyes, optical nerves, and the majority of the brain is verified.

In radiotherapy treatment, the number of particles and the radiation dose is 2-3 orders of magnitude greater than that for imaging, producing high SNR images even with FBP reconstruction. The differences between the ground truth and the reconstructed images are largely due to a low detection resolution in the patient's superior-inferior direction. The ground truth was computed with a 0.25cm resolution in this direction, while the P²T images are effectively weighted-sums of multiple image slices due to the 10 cm detector height. Note that although current radiotherapy treatment combines multiple pencil beams as an aperture for

efficient delivery, SPB is a viable option with existing hardware using Multileaf Collimator (MLC)³⁰, or with a magnetic scanning beam system under development³¹.

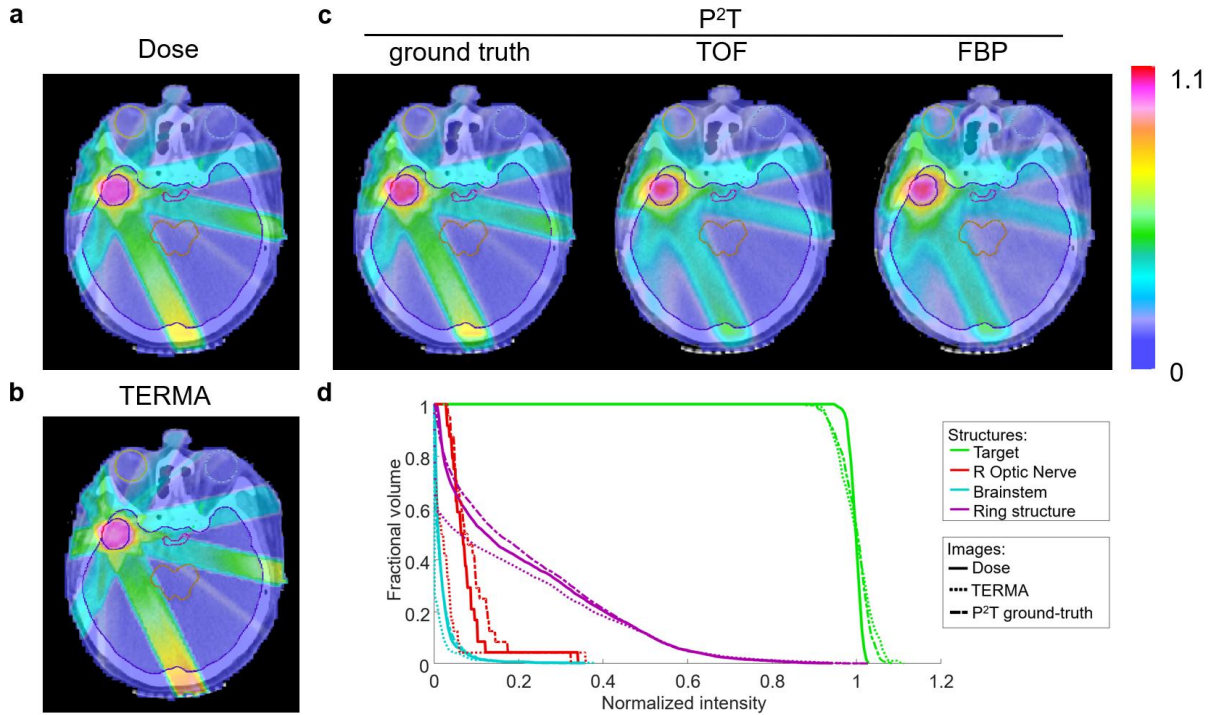


Figure 5 The (a) dose, (b) TERMA, and (c) P²T images of the radiotherapy treatment for a GBM patient using 10MV x-ray beams and Intensity-Modulated Radiotherapy (IMRT) delivery technique. All images were displayed as iso-intensity color-wash images superimposed on the CT image. The target and the normal tissues are contoured with different colors. All images were normalized by the mean intensity value within the target. (d) The cumulative Intensity Volume Histograms (cIVHs) of dose, TERMA, and P²T ground truth. The cIVH lines indicate the volume percentage of a structure receiving intensity values higher than a threshold.

Discussion

We report a completely novel X-ray tomography method, P²T. Owing to the distinct imaging formation mechanism based on high energy X-ray pair production, P²T provides three unique features that are evidently beyond X-ray CT's capabilities. First, the P²T image intensity is linear to the atomic number after fluence correction, disambiguating the difficult atomic number mapping task. Moreover, the linearity to effective atomic numbers leads to a remarkable increase in P²T contrast for certain low atomic number soft tissues, overcoming a CT's major weakness. Second, unlike CT that generally exposes a large volume to imaging dose from many angles, P²T can image a partial volume with as few as one beam (the sparse-view study used only two beams and 20% of the full-view) allowing unprecedented control over the imaging dose distribution. Third, P²T intensities are closely related to dose for in vivo dosimetry. Unlike X-ray induced radiation acoustic imaging³² or Cerenkov imaging¹⁵, in-vivo dosimetry using P²T is not limited

by anatomical locations and acoustic boundaries. These highly generalizable new features can profoundly influence a broad range of detection and diagnosis applications.

Despite that P²T is reported for the first time, its acquisition is within the realm of existing technologies. P²T benefits from decades of technological development of PET, which provides the energy and timing windows to remove non-pair production photon contamination. Moreover, for emission guided radiotherapy, the integration of a high energy source and a PET detector ring was recently demonstrated³³.

We implemented three reconstruction methods for P²T. Among them, the SPB and TOF methods result in significantly higher Signal-to-Noise Ratios (SNRs) compared with the FBP method. TOF relies heavily on the time resolution of the detector, requiring a 20 ps time resolution to localize the annihilation event within an accuracy of 3 mm. The 20 ps time resolution detector is consistent with the roadmap of PET detection using prompt Cherenkov emission^{19,20} or ultrafast emitting quantum-confined systems^{34,35}, although both still require significant engineering development to be practical³⁶. On the other hand, the SPB significantly relaxes the required time resolution due to the known excitation path. We assumed 300 ps time resolution for the SPB based and FBP reconstruction, which is commercially available for PET²¹. The sequential pencil beams required for SPB are also feasible with current technologies, such as Multileaf collimator (MLC)³⁰ or scanning photon beams³¹.

Method

Detection signal simulation

We assumed that the primary photons within each pencil beam are released from the source following a uniform distribution with an averaged releasing rate R . The time of the incident photon generation t_{incident} is:

$$t_{\text{incident}}(n, b) = t_{\text{incident}}(n - 1, b) + \tilde{t}, \quad \tilde{t} \sim U(0, 2/R)$$

where n is the index of the released primary photon, b is the index of the pencil beam. In the volume imaging, the first primary photons of all pencil beams are released altogether. In SPB imaging, the first primary photon of one pencil beam only starts after all photons are released in the previous pencil beam.

When a qualifying photon (within the energy resolution window) passes through the ring-detector, the colliding detector module records the traveling time t_{travel} of the detection event since the primary photon was generated and departed from the source, based on the MC simulation in Geant4. The global time t_{global} of the detection is then computed by adding the traveling time t_{travel} to the generation time of the corresponding incident photon t_{incident} :

$$t_{\text{global}} = t_{\text{incident}} + t_{\text{travel}}.$$

The detector response time t_{response} is simulated as a Gaussian distribution with variance $\sigma^2 = \Delta T^2$, where ΔT is the time resolution of the detector. The simulated detection time $t_{\text{detection}}$ of the photon is:

$$t_{\text{detection}} = t_{\text{global}} + t_{\text{response}}, \quad t_{\text{response}} \sim N(0, \Delta T^2)$$

For each beam, the detected signals were discarded for all detector modules receiving primary photons, due to the difficulty of identifying the annihilation photons from the primary photons with energy near 511 keV.

Some simplifications in detector geometry and properties were made in this study. The radiation source was not modeled for simplicity. We also assumed an ideal ring-detector that records the signal when the photon arrives at the detector. In reality, the photon may travel through a few detector modules before generating a signal, causing parallax error. The parallax error could be avoided with a more advanced detector using Depth-of-Interaction (DOI) information^{37,38}. Despite assuming an ideal detector response, the SNRs of the reconstructed images are still significantly lower than the ground-truth P²T images. The low SNR can be attributed to a wide detector module (a single detector module is 10cm long in the patient longitudinal direction) and an extremely low detector geometry efficiency: The ring detector only covers 4.17% of the 4π space, leading to only $(4.17\%)^2=0.17\%$ efficiency for collecting coincident photon pairs. Using detectors with multiple rows and extending the longitudinal coverage to 2m (such as in the EXPLORER project for total-body PET scanner³⁹) could improve the image resolution and raise the detector geometry efficiency by two orders of magnitude. These improvements are expected to significantly improve the SNR, shorten the imaging time, and reduce the radiation dose.

We used the general-purpose Monte Carlo package Geant4¹⁸ to study the P²T performance. Geant4 includes numerous well-validated physical models and is flexible for different applications. To accelerate the simulation, we developed an automated and distributed computation framework that allows asynchronous and scalable computation divided at the unit of individual pencil beams. A total of over 280 logical CPU cores were utilized for simulation. The simulation time for the full-view phantom simulation, partial-view phantom simulation, and radiotherapy imaging simulation are 30 hours, 7 hours, and 6 days, respectively. Further acceleration may be achieved by using the graphic processing unit (GPU) based MC code with simplified physical models⁴⁰.

Filtered Back Projection (FBP) reconstruction

From the simulated detector signals, coincident events were identified as two energy-eligible photons (within the energy window) arriving at two detector modules within the coincidence

time $t_{\text{coincidence}}$. Two coincident events define a Line-Of-Response (LOR): the line connecting the two detector modules, indicating that the annihilation event happened on the LOR.

With all LORs identified, a rebinning algorithm was applied to convert the list-mode pair-wise detector data to the sinogram data. The list-mode data of 1440 detectors were histogrammed into sinograms having 227 radial bins and 1440 angles. Filtered Back Projection (FBP) reconstruction was applied on the sinogram data using the Michigan Image Reconstruction Toolbox (MIRT)²², where a plain ramp filter was applied on the Fourier Transform of the sinogram at each angle before applying an Inverse Fourier Transform and back projection.

SPB based reconstruction

With SPB imaging, the locations of annihilation events can be further tracked down to the area where the incident beam passes through. The SPB based reconstruction was applied to the list-mode pair-wise detector data. For each detector pair, the intersection of the corresponding LOR and SPB locates the annihilation event. The SPB based reconstruction tallies the intersections within each voxel from all detector-pair data. Each intersection point is locally convolved with a Gaussian kernel to reduce image noises and artifacts.

Time-of-flight reconstruction

For detectors with a high time resolution (e.g., 20 ps), the location of the annihilation event can be computed from the flying time of the two photons. The traveling distance difference Δd between the two photons is $\Delta d = c \cdot \Delta t$, where c is the speed of light, and Δt is the time difference of the two photons when arriving at the detectors. The location of the annihilation event on the LOR can then be derived from the traveling distance difference Δd . The located point is locally convolved with a Gaussian kernel to reduce image noises and artifacts. Note that the image resolution $\Delta R = c\Delta T/2$ is limited by the detector time resolution ΔT .

Attenuation Correction

Before arriving at the detectors, the two coincident photons may be absorbed or scattered as they travel through the imaging subject. To compensate for the attenuation, the detector data needs to be corrected accordingly.

For FBP, the attenuation correction was performed on the sinogram:

$$P_c(i) = P_r(i) \cdot \exp\left(\int_i \mu_{511} dl\right),$$

where P_c is the corrected sinogram, and P_r is the raw sinogram obtained directly from the list-mode detector data. i is the index of the sinogram. μ_{511} is the attenuation coefficients of the imaging subject for 511 keV x-ray. The attenuation correction factor $\exp\left(\int_i \mu_{511} dl\right)$ is an

integral over the path of the coincident photons associated with the i^{th} element of the sinogram. After the attenuation correction, the corrected sinogram P_c is used for FBP reconstruction.

For SPB based method and the TOF method, the attenuation correction factor is computed as the same line integral over the path of the coincident photons. During reconstruction, the voxel-wise tallies are weighted by the correction factor of each identified detector-pair.

Fluence correction for quantitative imaging

The total nuclear pair-production cross-section per atom α_a is¹⁷:

$$\alpha_a = \sigma_0 Z^2 \int_0^1 P d \left(\frac{T^+}{h\nu - 2m_0 c^2} \right) = \sigma_0 Z^2 \bar{P} \approx Z^2$$

where T^+ is the positron energy, $h\nu$ is the energy of the incident photon, Z is the atomic number, P is a function of $h\nu$ and Z , m_0 is the mass of electron and positron, σ_0 is a constant.

The attenuation coefficient α of nuclear pair-production is therefore proportional to the atomic number Z and density ρ :

$$\alpha = \rho \alpha_a \frac{N_A}{A} \propto \rho Z,$$

where a simplification was made using the property that Z/A is close to 1 for most elements.

The P²T image signal is proportional to the attenuation coefficient of the imaging material and the x-ray fluence intensity f :

$$I \propto f \alpha \propto f \rho Z$$

The fluence intensity at image voxel v from pencil beam b is

$$f_{v,b} = f_{r,b} \cdot \frac{(p_r - p_s)^2}{(p_v - p_s)^2} \cdot \exp \left(- \int_{p_s}^{p_v} \mu_{10MV} dl \right)$$

where p_s , p_v , and p_r are the locations of the source, image voxel v , and a reference point r respectively. The reference point r is outside the imaging subject and on the line segment connecting the source and the voxel v . $f_{r,b}$ is the fluence intensity at the reference point from pencil beam b , and $f_{v,b}$ is the fluence intensity at image voxel v from pencil beam b . μ_{10MV} is the attenuation coefficients of the imaging subject for 10MV x-ray. The integral is computed using Siddon's ray tracing algorithm⁴¹ with the matRad toolbox⁴².

The total fluence intensity at image voxel v is

$$f_v = \sum_b f_{v,b}.$$

The dependence of the image intensity on the incident x-ray fluence intensity can be removed with the fluence correction. The corrected image intensity \tilde{I} is proportional to the product of density and the atomic number, obtained by voxelwise scaling of the P²T image by the fluence intensity f :

$$\tilde{I}_v = I_v/f_v \propto \rho_v Z_v.$$

Note that the fluence correction is only performed for quantitative imaging applications, and it does not apply to the P²T images obtained during radiotherapy treatments.

P²T image contrast for compounds

The Bragg's additivity rule applies to the pair production mass attenuation coefficient of compounds $\left(\frac{\alpha}{\rho}\right)_{comp}$:

$$\left(\frac{\alpha}{\rho}\right)_{comp} = \sum_i \left(\frac{\alpha}{\rho}\right)_i f_i$$

where f_i and $\left(\frac{\alpha}{\rho}\right)_i$ are the weight fraction and the pair production mass attenuation coefficient of element i , respectively. After fluence correction, the P²T image intensity \tilde{I} is proportional to the pair production attenuation coefficient of compounds $(\alpha)_{comp}$. Using the property that $\left(\frac{\alpha}{\rho}\right)_i \propto Z_i$, then

$$\tilde{I} \propto (\alpha)_{comp} \propto (\rho)_{comp} \sum_i Z_i f_i,$$

where Z_i is the atomic number of element i , and $(\rho)_{comp}$ is the density of the compounds. Let Z_{eff} be the effective atomic number

$$Z_{eff} = \sum_i Z_i f_i,$$

Then the P²T image intensity \tilde{I} is proportional to $(\rho)_{comp} Z_{eff}$:

$$\tilde{I} \propto (\rho)_{comp} Z_{eff}.$$

Therefore, $(\rho)_{comp} Z_{eff}$ provides a theoretical estimate of P²T image contrast.

The material composition⁴³, density, and effective atomic number of the 10 inserts in the standard phantom are listed in Table 2.

Tissue	Composition (%)												ρ (g cm ⁻³)	Z_{eff}	
	H	C	N	O	Na	Mg	P	S	Cl	K	Ca	Fe			
Air			70.0	30.0										0.001	7.3
Lung inhale	10.3	10.5	3.1	74.9	0.2		0.2	0.3	0.2	0.3				0.22	7.16
Lung exhale	10.3	10.5	3.1	74.9	0.2		0.2	0.3	0.2	0.3				0.51	7.16
Adipose	11.4	59.8	0.7	27.8	0.1			0.1	0.1					0.97	6.02
Breast	10.9	50.6	2.3	35.8	0.1		0.1	0.1	0.1					0.99	6.24
Water	11.2			88.8										1.00	7.22
Muscle	10.2	14.3	3.4	71.0	0.1		0.2	0.3	0.1	0.4				1.06	7.09
Liver	10.2	13.9	3.0	71.6	0.2		0.3	0.3	0.2	0.3				1.07	7.13
Trabecular	8.5	40.4	5.8	36.7	0.1	0.1	3.4	0.2	0.2	0.1	4.4	0.1		1.16	7.89
Dense Bone	5.6	23.5	5.0	43.4	0.1	0.1	7.2	0.3	0.1	0.1	14.6			1.58	10.48

Table 2 Material composition, density, and effective atomic number of the 10 inserts in the standard phantom, including air, lung inhale, lung exhale, adipose, breast, water, muscle, liver, trabecular bone, and dense bone.

Radiotherapy dose and pair production tomography imaging (P²T)

The radiotherapy dose is closely related to a concept named TERMA, the Total Energy Released per unit Mass. TERMA is defined for photons as

$$\text{TERMA} = \int f(E)E \frac{\mu(E)}{\rho} dE$$

where f is the fluence intensity, E is the photon energy, ρ is the material density, and μ is the attenuation coefficient, including contributions from Rayleigh, photoelectric, Compton, and pair production interactions.

Radiation dose can be computed by convolving TERMA with energy deposition kernels using the collapsed cone convolution (CCC) algorithm²⁹ to account for the dose spread under different materials and photon energies.

The P²T image collected during radiotherapy is also proportional to the fluence intensity (no fluence correction applied):

$$I \propto \int f(E)\alpha(E)dE$$

where $\alpha(E)$ is the pair production attenuation coefficient.

Most human tissues are approximately water-equivalent under the high energy X-rays used in radiotherapy. Therefore, the P²T image intensity and the TERMA are proportional to the fluence

intensity. Subsequently, the P²T image is strongly correlated with the dose distribution and can be used for in-vivo dose monitoring.

Code Availability Statement

We used the open source Monte Carlo code GEANT4 for simulation.

<https://geant4.web.cern.ch/node/1>

We used the open source CT reconstruction code for FBP reconstruction:

<https://web.eecs.umich.edu/~fessler/code/>

We will make the phantom and anonymized patient data available to the public for free access. We will upload the reconstruction code for the SPB and TOF to GitHub for open access prior to paper publication. Interested researchers should be able to reproduce the entirety of our study with provided data and code.

References

1. Smith, F. W. *et al.* Oesophageal carcinoma demonstrated by whole-body nuclear magnetic resonance imaging. *Br. Med. J. (Clin. Res. Ed)*. (1981). doi:10.1136/bmj.282.6263.510
2. Hawkes, R., Holland, G., Moore, W. S. & Worthington, B. Nuclear Magnetic Resonance (NMR) Tomography of the Brain: A Preliminary Clinical Assessment with Demonstration of Pathology. *J. Comput. Assist. Tomogr.* (1980). doi:10.1097/00004728-198010000-00001
3. Moore, E. A. Magnetic resonance imaging. in *Physics for Diagnostic Radiology: Third Edition* (2011). doi:10.1017/s0266462300001501
4. Shukla, A. & Kumar, U. Positron emission tomography: An overview. *Journal of Medical Physics* (2006). doi:10.4103/0971-6203.25665
5. Kalender, W. A. X-ray computed tomography. *Physics in Medicine and Biology* (2006). doi:10.1088/0031-9155/51/13/R03
6. Geise, R. A. Computed Tomography: Physical Principles, Clinical Applications, and Quality Control. *Radiology* (1995). doi:10.1148/radiology.194.3.782
7. Cormack, A. M. Representation of a function by its line integrals, with some radiological applications. II. *J. Appl. Phys.* (1964). doi:10.1063/1.1713127
8. Oldendorf, W. H. Isolated Flying Spot Detection of Radiodensity Discontinuities—Displaying the Internal Structural Pattern of a Complex Object. *Ire Trans. Biomed. Electron.* (1961). doi:10.1109/TBMEL.1961.4322854
9. Rubin, G. D. Computed tomography: Revolutionizing the practice of medicine for 40 years. *Radiology* (2014). doi:10.1148/radiol.14141356

10. Shen, L., Zhao, W. & Xing, L. Patient-specific reconstruction of volumetric computed tomography images from a single projection view via deep learning. *Nat. Biomed. Eng.* (2019). doi:10.1038/s41551-019-0466-4
11. Zhang, Z., Liang, X., Dong, X., Xie, Y. & Cao, G. A Sparse-View CT Reconstruction Method Based on Combination of DenseNet and Deconvolution. *IEEE Trans. Med. Imaging* (2018). doi:10.1109/TMI.2018.2823338
12. Sidky, E. Y., Lorente, I., Brankov, J. G. & Pan, X. Do CNNs solve the CT inverse problem? *arXiv* (2020). doi:10.1109/tbme.2020.3020741
13. Page, B. R. *et al.* Cobalt, linac, or other: What is the best solution for radiation therapy in developing countries? *Int. J. Radiat. Oncol. Biol. Phys.* (2014). doi:10.1016/j.ijrobp.2013.12.022
14. Black, R. D. *et al.* An analysis of an implantable dosimeter system for external beam therapy. *Int. J. Radiat. Oncol. Biol. Phys.* (2005). doi:10.1016/j.ijrobp.2005.05.025
15. Axelsson, J., Davis, S. C., Gladstone, D. J. & Pogue, B. W. Cerenkov emission induced by external beam radiation stimulates molecular fluorescence. *Med. Phys.* (2011). doi:10.1118/1.3592646
16. Xiang, L. *et al.* X-ray acoustic computed tomography with pulsed x-ray beam from a medical linear accelerator. *Med. Phys.* (2013). doi:10.1118/1.4771935
17. Attix, F. H. *Introduction to Radiological Physics and Radiation Dosimetry. Introduction to Radiological Physics and Radiation Dosimetry* (1986). doi:10.1002/9783527617135
18. Agostinelli, S. *et al.* GEANT4 - A simulation toolkit. *Nucl. Instruments Methods Phys. Res. Sect. A Accel. Spectrometers, Detect. Assoc. Equip.* (2003). doi:10.1016/S0168-9002(03)01368-8
19. Ota, R. *et al.* Coincidence time resolution of 30 ps FWHM using a pair of Cherenkov-radiator-integrated MCP-PMTs. *Phys. Med. Biol.* (2019). doi:10.1088/1361-6560/ab0fce
20. Ariño-Estrada, G. *et al.* Towards time-of-flight PET with a semiconductor detector. *Phys. Med. Biol.* (2018). doi:10.1088/1361-6560/aaaa4e
21. Hsu, D. F. C. *et al.* Studies of a Next-Generation Silicon-Photomultiplier–Based Time-of-Flight PET/CT System. *J. Nucl. Med.* **58**, 1511 LP – 1518 (2017).
22. Fessler, J. A. Michigan Image Reconstruction Toolbox, available at <https://web.eecs.umich.edu/~fessler/code/>.
23. White, D. R., Booz, J., Griffith, R. V, Spokas, J. J. & Wilson, I. J. Report 44. *J. Int. Comm. Radiat. Units Meas.* **os23**, NP-NP (1989).
24. Tuy, H. K. INVERSION FORMULA FOR CONE-BEAM RECONSTRUCTION. *SIAM J. Appl. Math.* (1983). doi:10.1137/0143035
25. Bortfeld, T. IMRT: A review and preview. *Physics in Medicine and Biology* (2006).

doi:10.1088/0031-9155/51/13/R21

26. Brahme, A., Roos, J. E. & Lax, I. Solution of an integral equation encountered in rotation therapy. *Phys. Med. Biol.* (1982). doi:10.1088/0031-9155/27/10/002
27. Nguyen, D. *et al.* Dose domain regularization of MLC leaf patterns for highly complex IMRT plans. *Med. Phys.* **42**, 1858 (2015).
28. Beck, A. & Teboulle, M. A fast iterative shrinkage-thresholding algorithm. *SIAM J. Imaging Sci.* **2**, 183 (2009).
29. Ahnesjö, A. Collapsed cone convolution of radiant energy for photon dose calculation in heterogeneous media. *Med. Phys.* (1989). doi:10.1118/1.596360
30. Jeraj, M. & Robar, V. Multileaf collimator in radiotherapy. *Radiol. Oncol.* (2004).
31. Maxim, P. G., Tantawi, S. G. & Loo Jr, B. W. PHASER: A platform for clinical translation of FLASH cancer radiotherapy. *Radiother. Oncol.* **139**, 28–33 (2019).
32. Zhang, W. *et al.* Dual-Modality X-Ray-Induced Radiation Acoustic and Ultrasound Imaging for Real-Time Monitoring of Radiotherapy. *BME Front.* (2020). doi:10.34133/2020/9853609
33. Shirvani, S. M. *et al.* Biology-guided radiotherapy: redefining the role of radiotherapy in metastatic cancer. *Br. J. Radiol.* **94**, 20200873 (2021).
34. Turtos, R. M. *et al.* Ultrafast emission from colloidal nanocrystals under pulsed X-ray excitation. *J. Instrum.* (2016). doi:10.1088/1748-0221/11/10/P10015
35. Tomanová, K. *et al.* On the structure, synthesis, and characterization of ultrafast blue-emitting CsPbBr₃ nanoplatelets. *APL Mater.* **7**, 11104 (2019).
36. Lecoq, P. *et al.* Roadmap toward the 10 ps time-of-flight PET challenge. *Physics in Medicine and Biology* (2020). doi:10.1088/1361-6560/ab9500
37. Ito, M., Hong, S. J. & Lee, J. S. Positron emission tomography (PET) detectors with depth-of-interaction (DOI) capability. *Biomedical Engineering Letters* (2011). doi:10.1007/s13534-011-0019-6
38. Mohammadi, I., Castro, I. F. C., Correia, P. M. M., Silva, A. L. M. & Veloso, J. F. C. A. Minimization of parallax error in positron emission tomography using depth of interaction capable detectors: Methods and apparatus. *Biomedical Physics and Engineering Express* (2019). doi:10.1088/2057-1976/ab4a1b
39. Cherry, S. R. *et al.* Total-body PET: Maximizing sensitivity to create new opportunities for clinical research and patient care. *J. Nucl. Med.* (2018). doi:10.2967/jnumed.116.184028
40. Jia, X., Gu, X., Graves, Y. J., Folkerts, M. & Jiang, S. B. GPU-based fast Monte Carlo simulation for radiotherapy dose calculation. *Phys. Med. Biol.* (2011). doi:10.1088/0031-9155/56/22/002

41. Siddon, R. L. Fast calculation of the exact radiological path for a three dimensional CT array. *Medical Physics* (1985). doi:10.1118/1.595715
42. Cisternas, E., Mairani, A., Ziegenhein, P., Jäkel, O. & Bangert, M. matRad – a multi-modality open source 3D treatment planning toolkit. in *IFMBE Proceedings* (2015). doi:10.1007/978-3-319-19387-8_391
43. Valentin, J. & Streffer, C. Basic anatomical and physiological data for use in radiological protection: Reference values - ICRP Publication 89. *Ann. ICRP* (2002). doi:10.1016/S0146-6453(03)00002-2

Acknowledgments

This research is supported in part by NIH Grants No. R44CA183390 and R01 CA230278.

Author Contributions

All authors contributed extensively to the work presented in this paper. K.S. conceived the study and designed the experiments. Q.L. designed and implemented the Monte Carlo modeling, image reconstruction, and result analysis, for P²T and CT. R.N. implemented the Monte Carlo modeling for dose calculation and the distributed CPU computing framework for acceleration. All authors discussed the results and implications and commented on the manuscript.

Figures

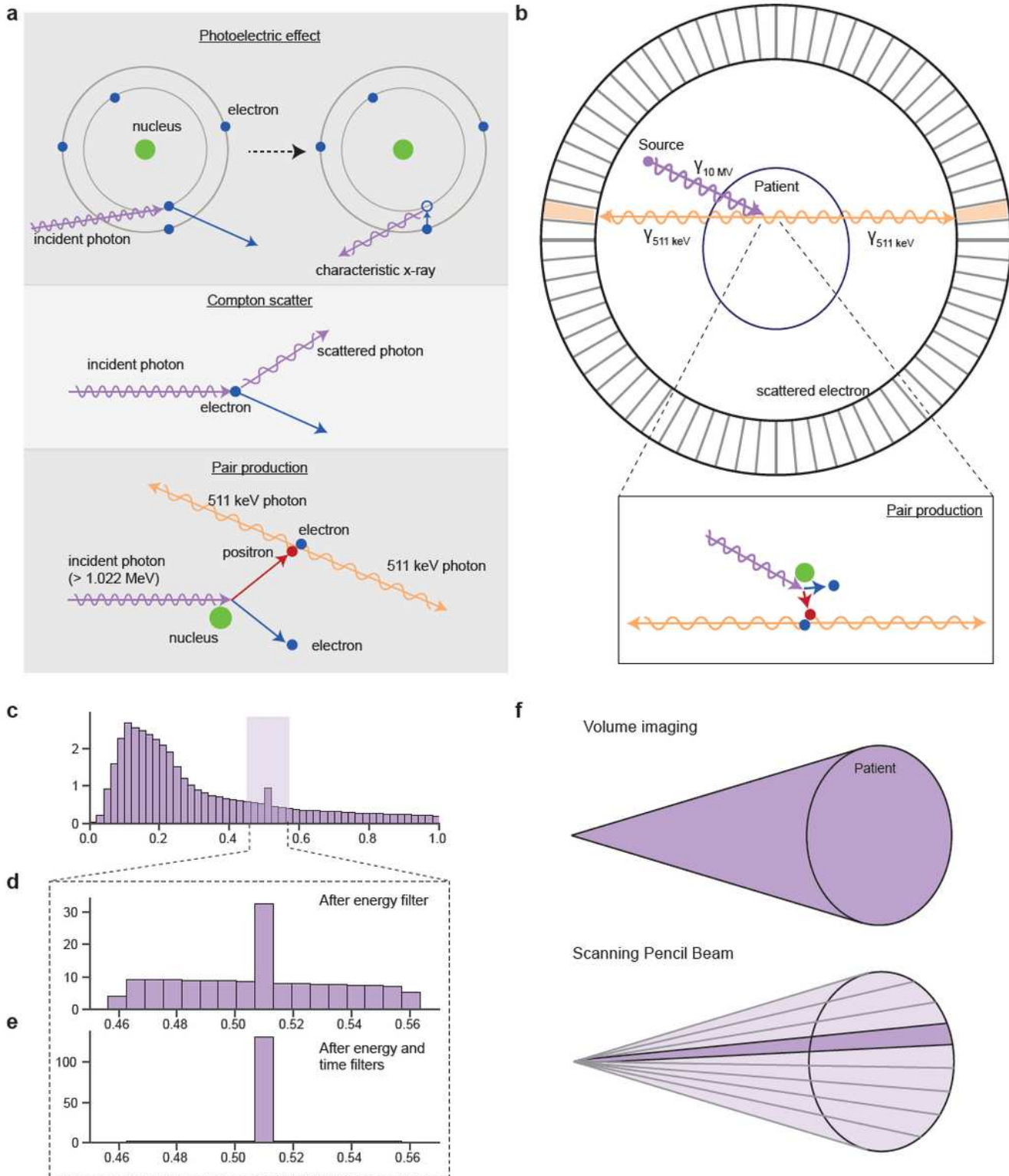


Figure 1

(a) Illustration of the photoelectric effect, Compton scatter, and pair production interaction. (b) Illustration of pair production tomography imaging (P2T) formation process. (c) The energy distribution of detected photons ranging from 0 to 1 MeV, (d) The energy distribution of detected photons after after applying an

$\pm 10\%$ energy window filter, (e) The energy distribution of detected photons and after applying the $\pm 10\%$ energy and 1 ns coincidence time filters. (f) Comparison of volume imaging and scanning pencil beam (SPB) imaging.

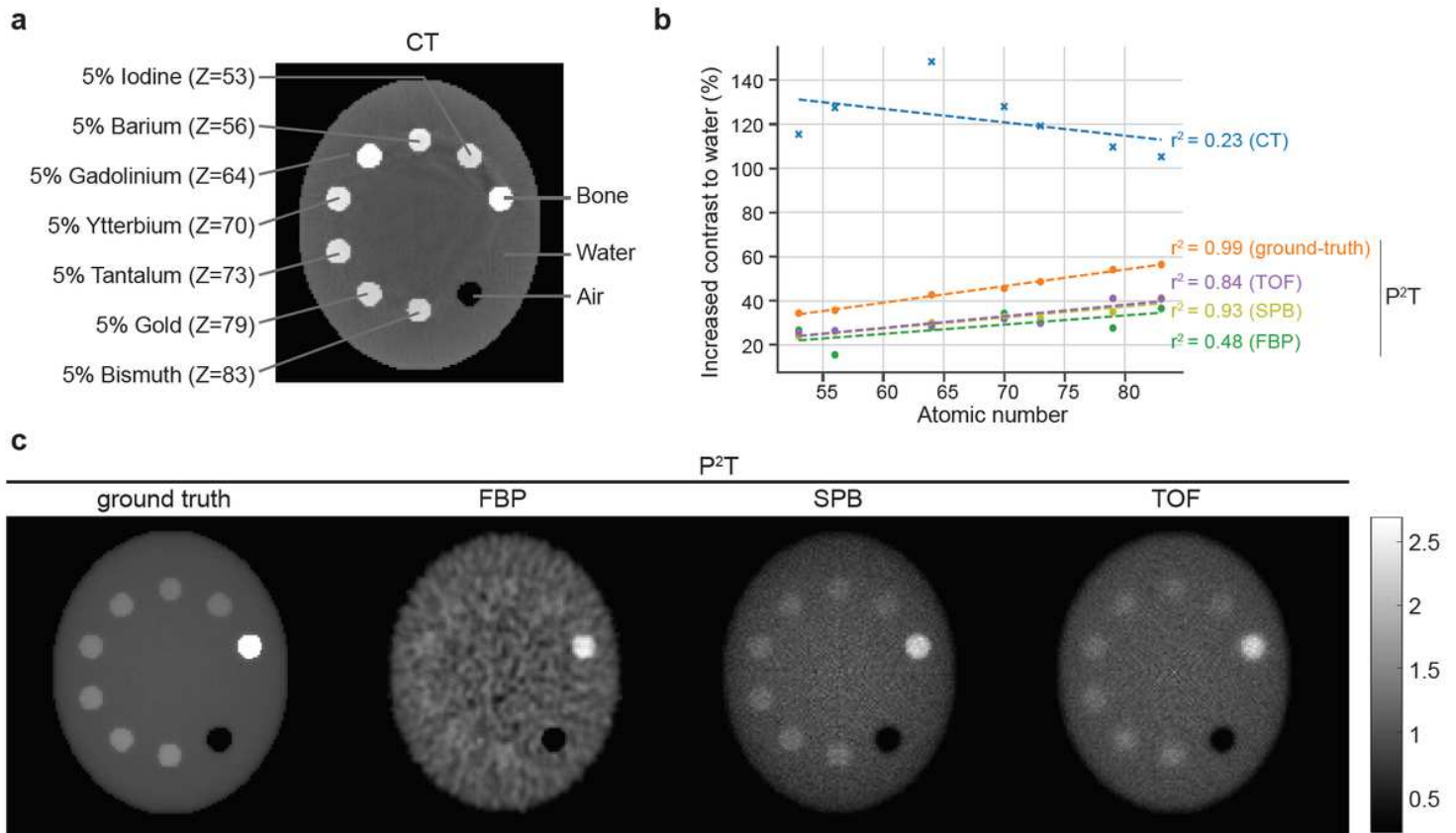


Figure 2

(a) The CT image of a nanoparticle phantom with 10 inserts, among which 7 inserts are made of water and 5% of high-Z elements, including Iodine, Barium, Gadolinium, Ytterbium, Tantalum, Gold, and Bismuth. (b) The relative increase in contrast to water is evaluated for the 7 inserts for the CT image and all P2T images. Linear regression of the increased contrast on the atomic number Z was performed for all images. (c) Comparison of P2T ground truth image, P2T image from FBP reconstruction, P2T image from SPB based reconstruction, and P2T image from TOF reconstruction. All images were normalized such that the intensity of the water insert is 1.

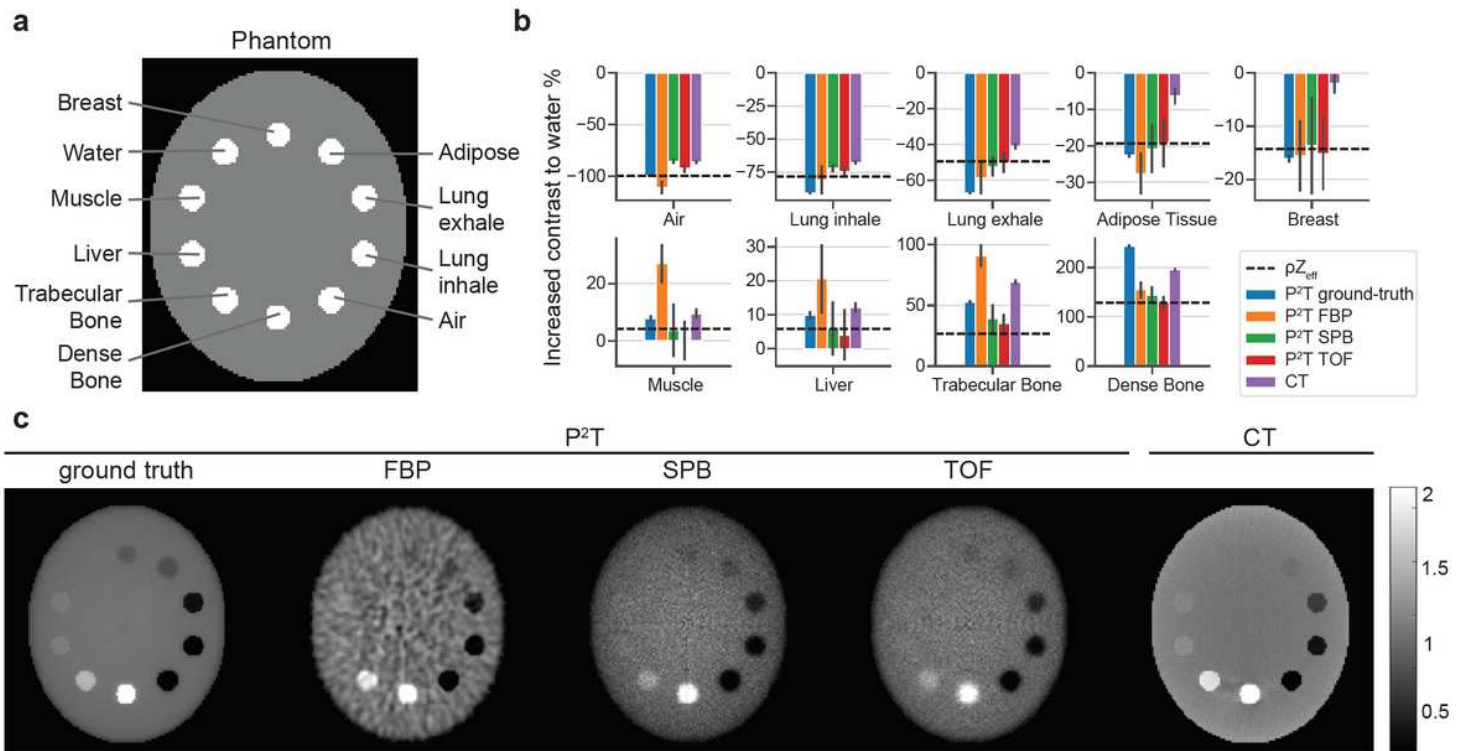


Figure 3

(a) The standard phantom with 10 inserts, including air, lung inhale, lung exhale, adipose, breast, water, muscle, liver, trabecular bone, and dense bone. (b) The relative increase in contrast to water is evaluated for all materials but water, with error bar showing standard deviations. The dashed lines show the increments in ρZ_{eff} of each material in relative to water. (c) Comparison of P2T ground truth image, P2T image from FBP reconstruction, P2T image from SPB based reconstruction, P2T image from TOF reconstruction, and CT image. All images were normalized such that the intensity of the water insert is 1.

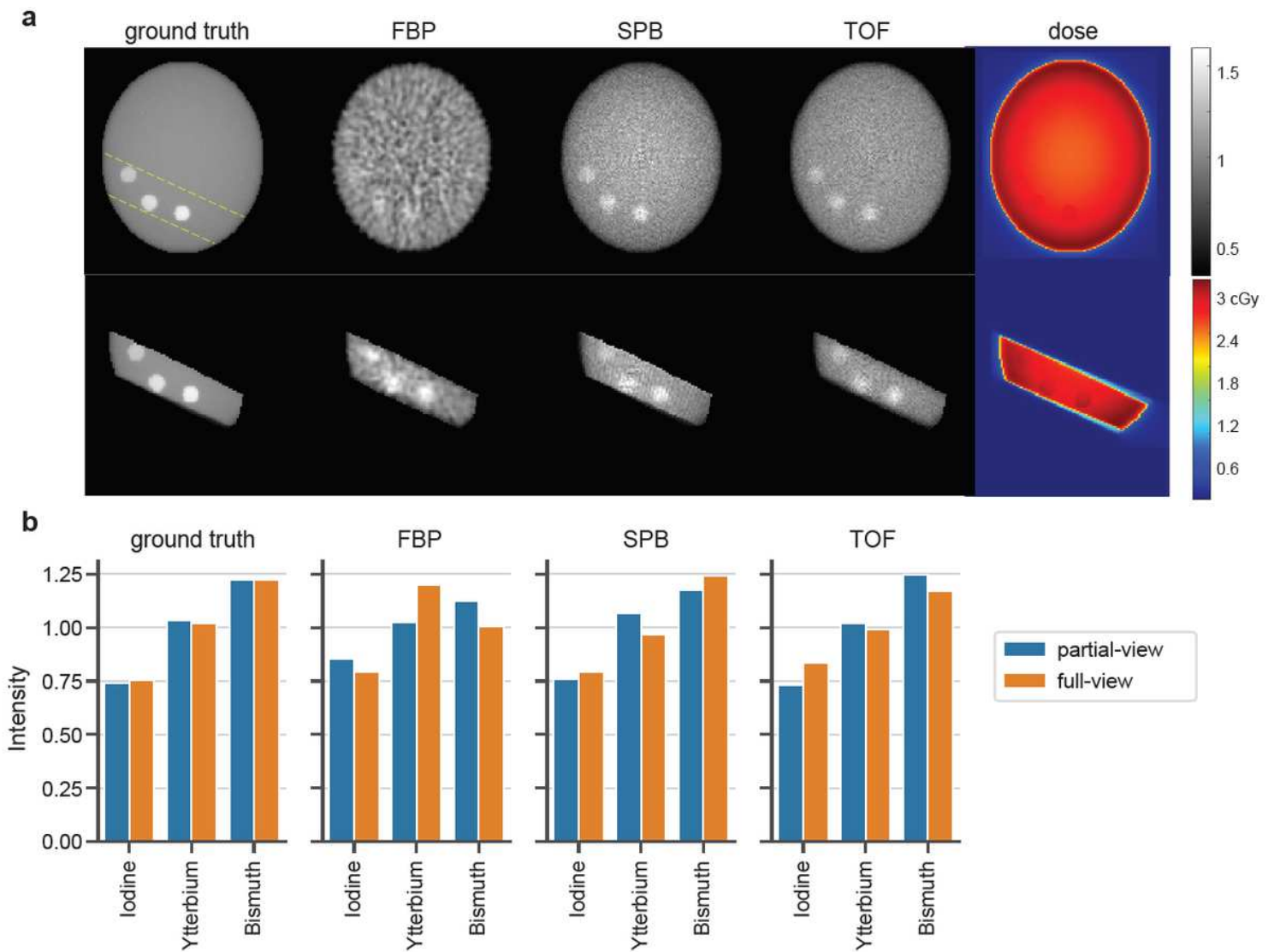


Figure 4

(a) Comparison of 20-beam full-view P2T images (top) and 2-beam partial-view P2T images (bottom), including ground truth image, P2T image from FBP reconstruction, P2T image from SPB based reconstruction, and P2T image from TOF reconstruction. All images were normalized such that the intensity of the water insert is 1. The three inserts in the partial-view are Iodine, Ytterbium, and Bismuth from left to right. (b) The image intensity of the 3 inserts normalized by their average values for both full-FOV P2T images and partial-view P2T images.

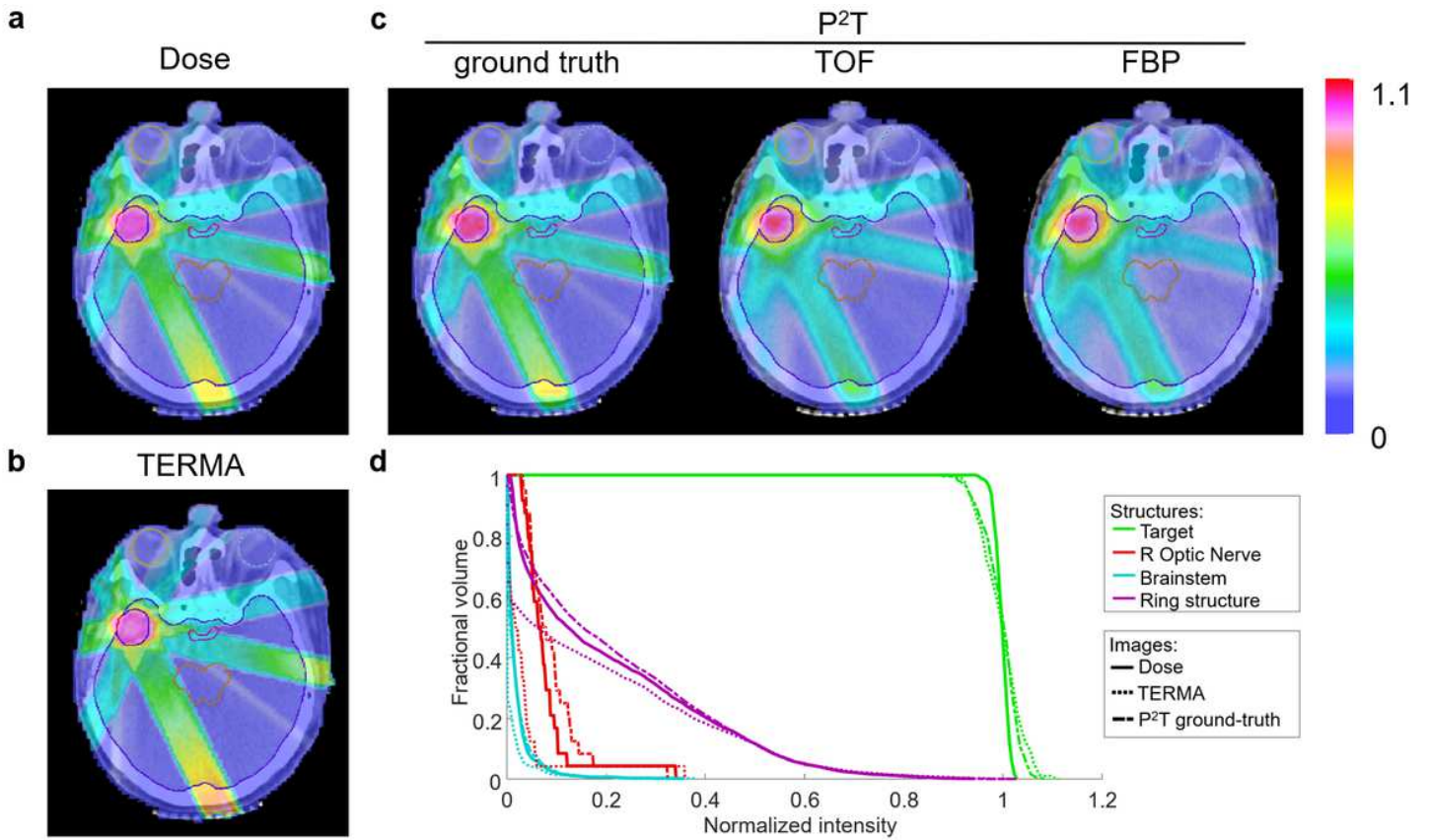


Figure 5

The (a) dose, (b) TERMA, and (c) P2T images of the radiotherapy treatment for a GBM patient using 10MV x-ray beams and Intensity-Modulated Radiotherapy (IMRT) delivery technique. All images were displayed as iso-intensity color-wash images superimposed on the CT image. The target and the normal tissues are contoured with different colors. All images were normalized by the mean intensity value within the target. (d) The cumulative Intensity Volume Histograms (cIVHs) of dose, TERMA, and P2T ground truth. The cIVH lines indicate the volume percentage of a structure receiving intensity values higher than a threshold.